Crustal structure beneath the Malawi and Luangwa Rift Zones and adjacent areas from ambient noise tomography

Tuo Wang [a], Jikun Feng [b], Kelly H. Liu [a], Stephen S. Gao [a,*]

[a] Geology and Geophysics Program, Missouri University of Science and Technology, Rolla, MO 65409, USA
[b] Laboratory of Seismology and Physics of Earth's Interior, School of Earth and Space Sciences, University of Science and Technology of China, Hefei 230026, China

ARTICLE INFO

ABSTRACT

Crustal shear wave velocity structure beneath the Malawi and Luangwa Rift Zones (MRZ and LRZ, respectively) and adjacent regions in southern Africa is imaged using fundamental mode Rayleigh waves recorded by 31 SAFARI (Seismic Arrays for African Rift Initiation) stations. Dispersion measurements estimated from empirical Green's functions are used to construct 2-D phase velocity maps for periods between 5 and 28 s. The resulting Rayleigh wave phase velocities demonstrate significant lateral variations and are in general agreement with known geological features and tectonic units within the study area. Subsequently, we invert Rayleigh wave phase velocity dispersion curves to construct a 3-D shear wave velocity model. Beneath the MRZ and LRZ, low velocity anomalies are found in the upper-most crust, probably reflecting the sedimentary cover. The mid-crust of the MRZ is characterized by an ~3.7% low velocity anomaly, which cannot be adequately explained by higher than normal temperatures alone. Instead, other factors such as magmatic intrusion, partial melting, and fluid-filled deep crustal faults might also play a role. Thinning of the crust of a few kilometers beneath the rifts is revealed by the inversion. A compilation of crustal thicknesses and velocities beneath the world's major continental rifts suggests that both the MRZ and LRZ are in the category of rifts beneath which the crust has not been sufficiently thinned to produce widespread syn-rifting volcanisms.

1. Introduction

Developed between the Proterozoic Irumide Belt and Pan-African South Irumide Belt (SIB), the Permo-Triassic Luangwa Rift Zone (LRZ; Fig. 1) is considered to be a section of the southwestern branch of the East African Rift System (EARS; Banks et al., 1995; Fritz et al., 2013). To the east of the LRZ lies the N-S oriented Malawi Rift Zone (MRZ), which is the southward extension of the non-volcanic western branch of the EARS and resides within the SIB and the Mozambique Belt (Ebinger et al., 1987; Craig et al., 2011; Lao-Davila et al., 2015). The earliest sediments (older than 4.0 Ma) in the MRZ are fluviatile deposits in the northern part of the rift (Flannery and Rosendahl, 1990; Betzler and Ring, 1995). The thickness of the sedimentary layers decreases gradually toward the south, from up to 3 km at the northern part of the rift to near zero at the southern end where the rift is floored by Precambrian rocks (Specht and Rosendahl, 1989). The MRZ is the youngest segment of the western branch of the EARS, initiated at about 14 million years ago (Roberts et al., 2012). Volcanism in the MRZ is absent except for the Rungwe volcanic province located at the northern tip of the rift (Ebinger et al., 1989).

Relative to most of the more mature rifts, young and incipient rifts such as the MRZ have been inadequately studied, and consequently, the mechanisms responsible for the initiation and early-stage development of continental rifts remain enigmatic. One of the proposed rifting models involves the active upwelling of thermal materials from the lower mantle to the upper mantle and crust, i.e., the active rifting model (e.g., Sengor and Burke, 1978). However, for the MRZ, a recent study (Reed et al., 2016) of the topography of the mantle transition zone discontinuities suggests the absence of thermal anomalies in the vicinity of the mantle transition zone, an observation that is inconsistent with the active rifting model. A lack of rifting-related mantle flow is also inferred from shear wave splitting analysis (Reed et al., 2017), which is expected to be characterized by either rift-parallel or orthogonal fast orientations (Gao et al., 1994, 1997). The measurements are also inconsistent with the existence of an active mantle plume. For an active mantle plume beneath a stationary (relative to the underneath mantle) lithosphere, the expected flow field and thus the fast orientations should have a radial pattern centered at the plume stem (Druken et al., 2013), and for a plume beneath a moving plate, the pattern is expected to be parabolic (Walker et al., 2001). The fast orientations
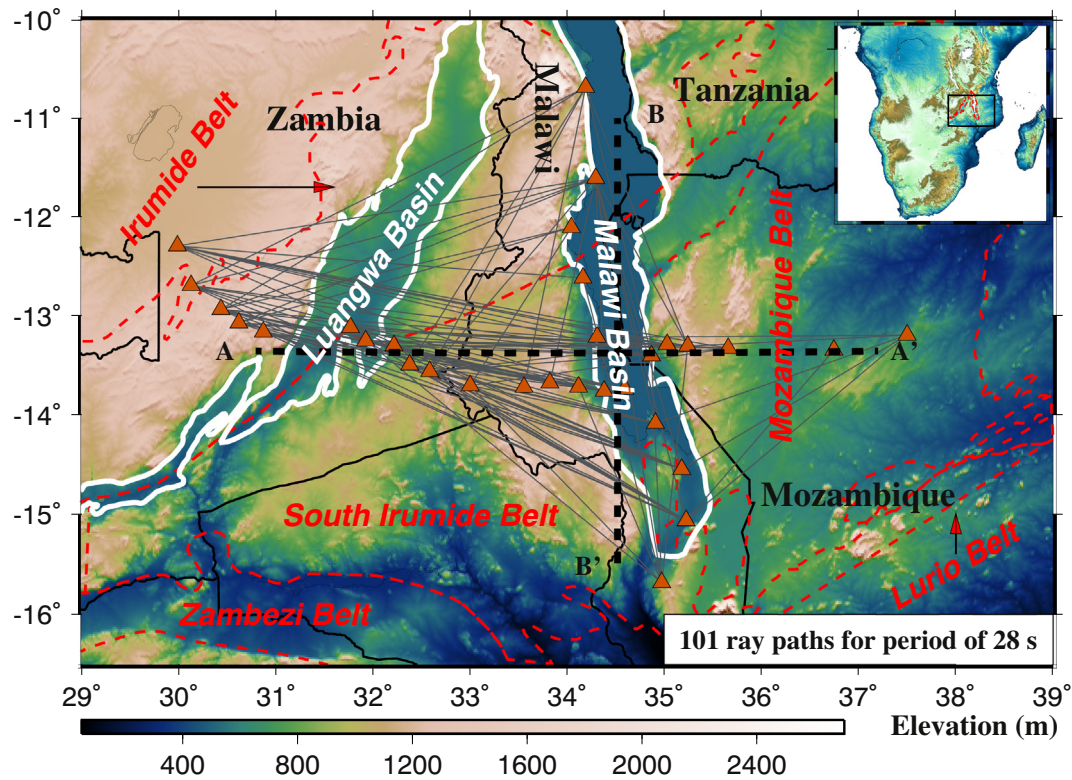
Fig. 1. Topographic map of the study region showing tectonic provinces and seismic stations used in this study (orange triangles). The gray lines represent 101 ray paths of station pairs that provide reliable phase velocity dispersion measurements at the period of 28 s. The red dashed lines depict the boundaries of major orogenic belts within the study area. The two black dashed lines, A–A′ and B–B′, are cross-sections shown in Figs. 8 and 9, respectively. (For interpretation of the references to color in this figure legend, the reader is referred to the web version of this article.)

observed in the vicinity of the MRZ and LRZ are mostly parallel to the absolute plate motion direction determined in the no-net-rotation reference frame, and thus there is no clear rifting or plume related flow field (Reed et al., 2017).

In the study area, the crustal thickness revealed in the global scale CRUST1.0 model (Laske et al., 2013), which has a coarse 1° by 1° horizontal resolution, varies from a minimum value of ~32 km at the central part of the MRZ to a maximum value of ~45 km in the southern part of the SIB. Higher resolution imaging of crustal velocity structure and crustal thickness variations can provide valuable constraints on the rifting models. Kim et al. (2009) estimated that the crustal thickness ranges from 34 ± 2 to 38 ± 2 km beneath the southeastern end of the Rukwa rift, which is located north of the study area, using teleseismic receiver functions. By applying the receiver function method and joint inversion of receiver functions and surface wave phase and group velocities, Kachingwe et al. (2015) estimated that the mean crustal thickness beneath the Irumide Belt and SIB is about 42 and 38 km, respectively. Tugume et al. (2012) calculated the average crustal thickness of the Mozambique Belt and found a value of ~38 km using receiver functions, and Borrego et al. (2018) utilized the receiver function and joint inversion analyses and suggested that the crustal thickness ranges from 38 to 42 km beneath the northern end of the Malawi rift.

Comparing with traditional surface-wave tomography methods for imaging crustal velocity structures, ambient noise tomography (ANT) has an improved inversion resolution by utilizing higher frequency surface waves, and by reducing the effects of the random occurrence of the sources and the inhomogeneous distribution of the receivers (e.g., Nolet and Dahlen, 2000; Spetzler et al., 2002; Ritzwoller et al., 2002; Shapiro and Campillo, 2004; Shapiro et al., 2005). The velocity structure at the northern tip of the MRZ has been revealed by Accardo et al. (2017) through ambient-noise and Rayleigh wave phase velocities. This study

expands the study area to the central and southern part of the MRZ and is the first ANT study of the combined region of the MRZ and LRZ. In this study, we obtain phase velocity maps at various periods by inverting phase velocity dispersion measurements from empirical Green's functions (EGFs). Additionally, to more directly image 3-D crustal structures, the phase velocities are inverted to construct a shear wave velocity model. Resulting crustal velocities and estimated crustal thicknesses beneath the MRZ and LRZ are then compared with those measured in other major continental rifts to reveal their relationship with the presence or absence of syn-rifting volcanisms.

2. Data and methods

2.1. Data

The broadband seismic data used in the study were recorded by 31 portable seismic stations, which are part of the Seismic Arrays for African Rift Initiation (SAFARI) experiment conducted between mid-2012 and mid-2014 (Gao et al., 2013). The data set has been archived at the Incorporated Research Institutions for Seismology (IRIS) Data Management Center (DMC) and is publicly accessible.

Equipped with Quanterra Q330 digitizers and Guralp CMG-3T 120 s sensors recording at a continuous rate of 50 Hz, the portable stations were located within the area of 29°E–39°E, and 16.5°S–10°S, along two profiles. The E-W profile is ~900 km long consisting of 21 stations in Zambia, Malawi, and Mozambique. It traversed both the MRZ and LRZ, approximately forming a right angle with the rifts (Fig. 1). The N-S profile is about 600 km long with 10 stations installed along the western shoulder of the MRZ except for the southernmost several stations which were approximately located along the rift axis (Fig. 1). We requested continuous vertical-component waveform data from the DMC

for the period of 1/1/2013 to 12/31/2013, each with a length of one day. The seismograms are resampled to 5 samples per second for the study.

2.2. Methods

The ANT technique has been discussed in detail by numerous studies (Weaver and Lobkis, 2004; Weaver, 2005; Shapiro and Campillo, 2004; Shapiro et al., 2005; Sabra et al., 2005). It is generally believed that ambient noise source would be more efficient in generating Rayleigh waves than Love waves. Additionally, uncertainties of phase velocity measurements are much smaller than those of group velocity measurements, and phase velocities have the ability to constrain deeper velocity structures than group velocities at the same periods (Lin et al., 2008). Therefore, in this study, we utilize the vertical component of cross-correlations of ambient seismic noise to retrieve Rayleigh wave phase velocity dispersion curves. The processing procedure that we use here includes four main steps: (1) preprocessing for single station, (2) cross-correlations and temporal stacking, (3) phase velocity dispersion measurements, and (4) phase velocity variations from EGFs and inversion for shear wave velocity structures.

2.2.1. Single station preprocessing

The primary purpose for single station preprocessing is to extract broadband ambient seismic noise. The procedure we use here is similar to that discussed in Bensen et al. (2007), and is briefly described below. After the mean, linear trend, and the instrumental response of the daily noise time series are removed, a second-order Butterworth filter in the frequency range of 0.025–0.5 Hz is applied. Subsequently, temporal normalization, which is regarded as the most important step in the preprocessing stage, is applied to reduce the effects from earthquakes, instrumental irregularities, and nonstationary noise around the stations. Spectral whitening is then applied to produce broader-band ambient noise signals by reducing broad imbalances in single-station spectra and to prevent degradation caused by persistent nearly monochromatic sources (Bensen et al., 2007).

2.2.2. Cross-correlation and temporal stacking

The next step is to compute cross-correlation series and perform temporal stacking. A daily cross-correlation between every station pair is performed to obtain a two-sided EGF. The total number of possible cross-correlation series is $N = n(n − 1)/2$, where n is the number of stations. Since there are 31 stations in total, 465 possible inter-station cross-correlation series are produced.

After the daily cross-correlations between all the station pairs are obtained, all the daily cross-correlation series for each of the station pairs are stacked to obtain a stacked cross-correlation series. The causal and acausal signals are symmetrically averaged to enhance the signal-to-noise ratio (SNR). Due to the heterogeneous distribution of the noise sources, the resulting cross-correlation functions are slightly asymmetrical. Finally, by taking a negative time derivative of the stacked cross-correlation series, the Rayleigh wave EGFs are obtained. Fig. 2 shows raypaths and cross-correlation series between station W01PD and all the other stations.

2.2.3. Phase velocity dispersion measurements

Based on a modified far-field approximation and an image transformation analysis technique (Yao et al., 2005, 2006, 2010), phase velocity dispersion curves are estimated from the EGFs. A quality control procedure is applied prior to computation of the dispersion curves to remove unreliable cross-correlation series, which are mainly caused by 1) the distance between the two stations in a station pair being either too long or too short, or 2) the quality of seismic data being not high enough.

Accordingly, we impose three selection criteria in order to obtain reliable dispersion measurements and to reject those contaminated by interference between the causal and acausal signals (Bensen et al., 2007). First, following the far-field approximation approach, the distance between the two stations in a given station pair should be at least three times of the longest wavelength, which is the product of the cut-off period and the corresponding phase velocity. In this study, the longest period of the dispersion measurements that we produced is 28 s, resulting in a minimum acceptable inter-station distance of 336 km for a typical phase velocity of 4 km/s (300 measurements are discarded by this criterion). Second, we calculate the SNR for every cross-correlation series and exclude phase velocity measurements with a SNR smaller than 5. The SNR here is defined as the ratio of the maximum amplitude within the signal window to the root-mean-square amplitude in a window of 150 s long following the signal window. Third, we perform clustering analysis to reject station pairs with large uncertainties in dispersion measurements (e.g., Ritzwoller and Levshin, 1998). Based on a similar cluster analysis in Bensen et al. (2007), we retain the phase velocity dispersion curves that are similar to a global model (Shapiro and Ritzwoller, 2002), and discard the ones with substantial velocity difference from the model prediction.
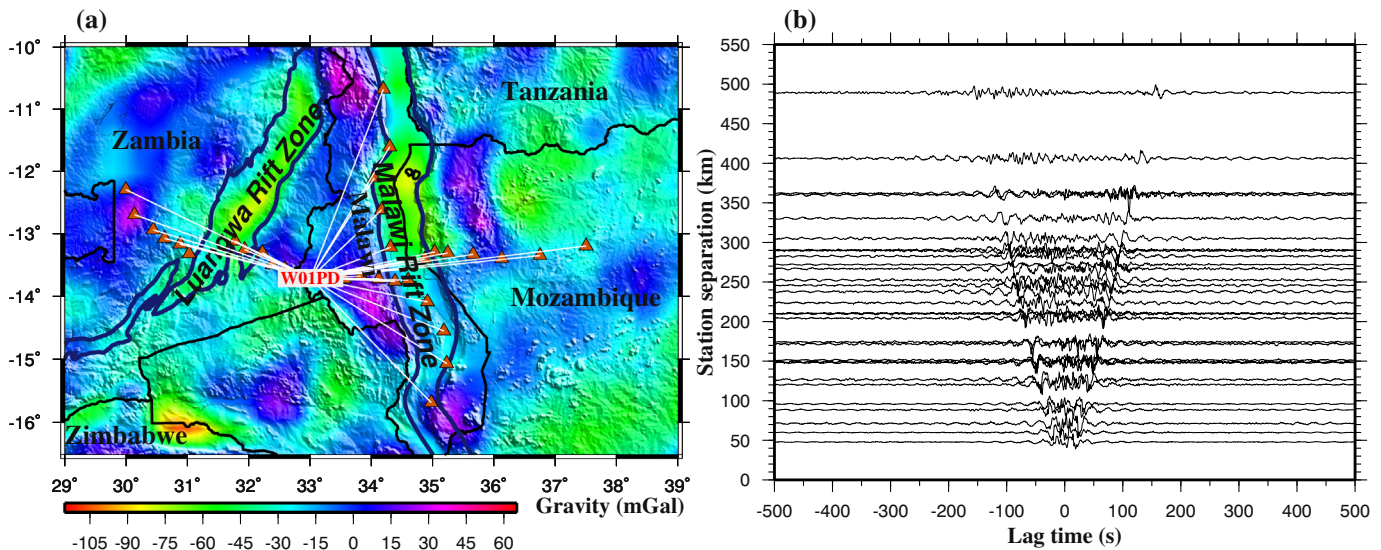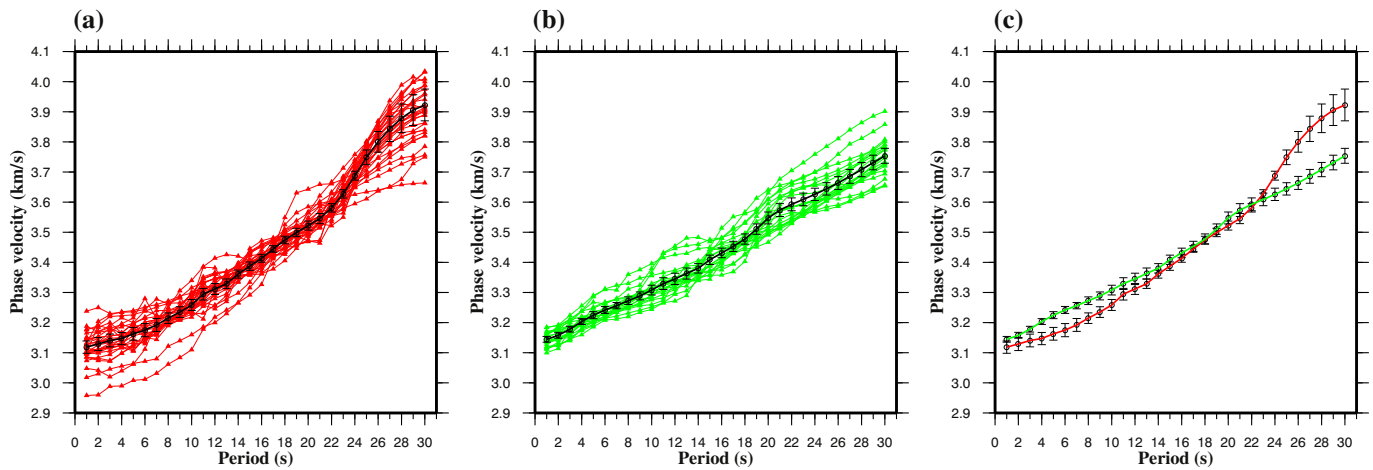

Fig. 2. (a) Bouguer gravity anomalies extracted from the World Gravity Map (WGM2012). The white lines show ray-paths of station W01PD with other stations. (b) 2–40 s band-pass filtered cross-correlation functions between station W01PD and the other stations.

Fig. 3. Examples of Rayleigh wave phase velocity dispersion curves. (a) 29 phase velocity dispersion curves for ray-paths traversing the MRZ (red) and the corresponding averaged phase velocity curve (black). The error bar shows one standard deviation. (b) Same as (a) but for 21 ray-paths that avoid the MRZ (green curves). (c) Comparison of the averaged phase velocity curves (red: traversing MRZ; green: off MRZ). (For interpretation of the references to color in this figure legend, the reader is referred to the web version of this article.)

Because EGF-derived phase velocity measurements are only robust enough in the period range of 5 to 28 s and become unreliable outside this range (Yao et al., 2006), measurements at periods shorter than 5 s and longer than 28 s are not used for generating the phase velocity maps in the next step. Examples of Rayleigh wave phase velocity measurements along different ray paths are shown in Fig. 3.

2.2.4. Phase velocity maps and inversion for shear wave velocities

Phase velocity measurements obtained from the previous step are inverted with the technique of Tarantola and Valette (1982) and Tarantola and Nercessian (1984) to obtain Rayleigh wave phase velocity maps for periods between 5 and 28 s with an interval of 1 s, a horizontal grid dimension of 0.12° × 0.12°, and a sampling step of 0.03°. In order to only display the area with relatively reliable phase velocities, the study area is meshed by squares of 0.12° × 0.12°, and only grids with at least one ray path are retained.

To create a 3-D shear wave velocity model of the study area, we next invert the phase velocity dispersion curve at each of the model nodes to obtain depth distribution of shear wave velocities at the nodes from the surface to 40 km depth by adopting the *surf96* computer program (Herrmann and Ammon, 2004). For constructing the initial model for the inversion, the layer thickness is fixed to be 1 km over the depth range, and initial crustal thicknesses are taken from the CRUST1.0 global model with the thickest crust of 45 km at the central part of the MRZ, the thinnest crust of 32 km at the northern part of the MRZ, and an average value of about 40 km. Densities and velocities are extracted from the IASP91 Earth model (Kennett and Engdahl, 1991). Low velocities in the top layers of the initial model are assigned to areas covered by water or a layer of loose sediments. The final 3-D shear wave velocity model is determined by integrating all the resulting shear velocity profiles.

3. Results

3.1. Phase velocity tomography

Based on the criteria discussed in Section 2.2.3, a total of 120 dispersion measurements are eventually selected from the 465 possible station pairs, and 2-D phase velocity maps with 0.12° × 0.12° spatial grids are constructed using the dispersion measurements. Fig. 4 shows phase velocity maps at the period of 5, 16, 20, and 28 s. The number of ray paths is 120, 119, 117, and 101, respectively, so that only minor changes for the ray-path coverages could be observed. Phase velocity sensitivity kernels for the above periods are calculated based on the IASP91 Earth model (Fig. 5a). The depth with the maximum sensitivity

is approximately 6, 20, 28, and 40 km, respectively, for the above periods. Sensitivity kernels are also calculated based on the IASP91 model with slight modifications to reflect loose sedimentary layers (Fig. 5b). The maximum sensitivity for the period of 5 s moves from 6 km to 7 km deep, and no influence of the low velocity layer is found for longer periods.

At the period of 5 s, the low phase velocities found in the MRZ and LRZ most likely reflect loose sediments and water, while relatively high velocities are revealed in the SIB between the two rifts and the Mozambique Belt east of the MRZ (Fig. 4). The low (relative to the SIB) velocities beneath both rifts persist at the period of 16 s. Continuing downward, at 20 s, velocities beneath the LRZ become comparable to those of the SIB, and low velocities beneath the MRZ are still present. At 28 s, the polarity of relative velocity contrast between the rifts and the SIB reverses. For all the periods, phase velocities beneath the SIB are comparable to those observed in other stable cratonic areas such as Central North America (e.g., Shen et al., 2013a, 2013b, and Shen and Ritzwoller, 2016).

3.2. Resolution test

To test the resolution of the resulting spatial distribution of phase velocities at different periods, standard synthetic checkerboard tests are conducted (Fig. 6). For each of the periods, the input velocity model is composed of alternating positive and negative velocity anomalies with a 5% magnitude relative to 4 km/s in 1.5° × 1.5° blocks (Fig. 6a).

Fig. 6b–e shows the recovered velocity models for the periods of 5, 16, 20, and 28 s obtained using the same ray-path coverage and inversion parameters as those used for inverting the observed data. The synthetic inversion results indicate that the reconstruction of the input model at different periods is understandably the best along the E-W and N-S trending arrays, because this is where crossing rays are dense (Fig. 1), and is generally poor in the off-profile areas due to limited ray coverage. Consequently, in the following we focus our discussions on results along the two profiles.

3.3. Shear wave velocity structures

According to the sensitivity kernels and initial models (Fig. 5), the phase velocity of Rayleigh waves is most sensitive to shear velocities (V_s) at the depth of about 1/3 of the wavelength (Yang et al., 2010). To more realistically reflect the velocity distribution at a given depth, we further invert phase velocities to obtain shear wave velocities and construct V_s maps at different depth using the procedure of Herrmann and
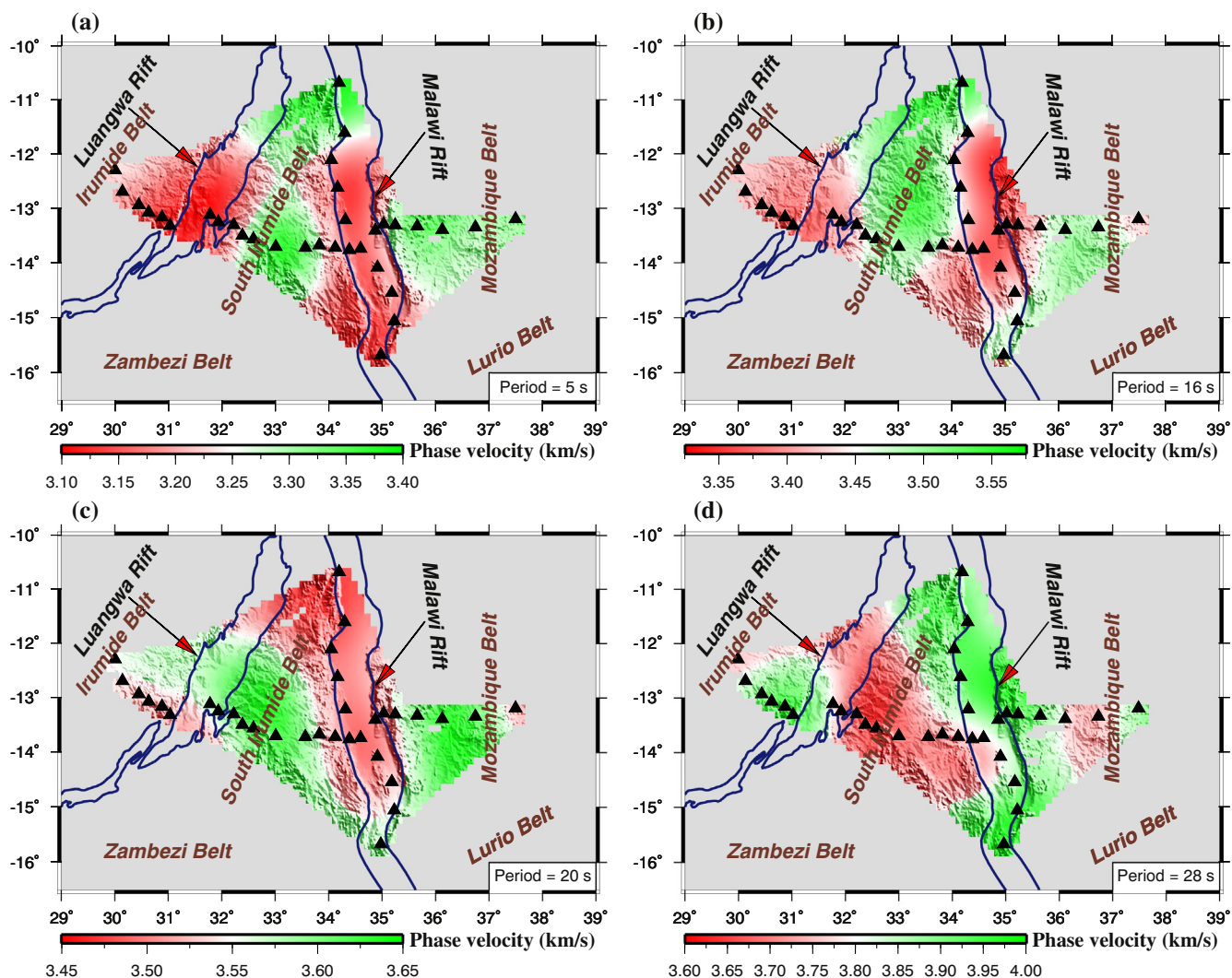
Fig. 4. Rayleigh wave phase velocity maps at the periods of 5, 16, 20, and 28 s. For each map, the period is labelled in the lower right corner, and the velocities are indicated by the scale bar.

Ammon (2004). The results are shown on 2-D horizontal slices (Fig. 7) and vertical profiles (Figs. 8 and 9). V_s variations with depth are also extracted at several representative locations to facilitate comparison (Figs. 8c and 9c).

Similar to the phase velocities (Fig. 4), the resulting shear velocities in the uppermost crust (0–5 km) beneath the MRZ are the lowest in the study area. Relative to the SIB, the observed V_s values are about 3.5% lower in the top 15 km beneath the MRZ (Fig. 8c). On the N-S trending vertical profile (Fig. 9b), the central MRZ demonstrates the lowest velocities in the top 15 km.

At greater depth in the mid-crust, low V_s anomalies are visible beneath the MRZ from horizontal velocity maps at depth slices of 20 and 28 km (Fig. 7b and c). The E-W trending profile (Fig. 8c) indicates that the MRZ is delineated by low velocities to about 30 km depth relative to the SIB, and in the depth range of 15–30 km, the southern and central MRZ have similar velocities (Fig. 9c).

In the depth range of 30 to 40 km, high V_s values relative to the SIB are pervasively found beneath the MRZ (Figs. 7 and 8). For instance, on the horizontal velocity slice at 40 km (Fig. 7d), V_s underneath the MRZ reaches 4.30 km/s. The sudden velocity increase with depth can also be observed on the extracted vertical velocity profiles for the MRZ (Figs. 8c and 9c). These velocities are higher than the globally-averaged lower-crustal shear wave velocity (3.75 km/s in the IASP91 Earth model).

Due to the available ray path coverage, only the central part of the LRZ has reliable V_s determinations. In the upper crust, the central LRZ is characterized by pronounced low-velocity anomalies relative to the SIB (Fig. 7a). On the vertical profiles, the V_s observations in the LRZ (Fig. 8c) are slightly higher than those beneath the MRZ for the depth range of 0–20 km, and are lower than those of the SIB from the surface to about 30 km. Similar to the MRZ, high velocities are revealed on the depth slice of 40 km depth beneath the LRZ (Fig. 7d).

4. Discussion

4.1. Causes of low crustal velocities beneath the MRZ and LRZ

The negative V_s anomalies observed in the top several kilometers beneath the MRZ (Fig. 7a) most likely reflect the 0.7 km water and the up to 3 km loose sedimentary layers (Betzler and Ring, 1995; Flannery and Rosendahl, 1990). Similarly, loose sediments in the LRZ may be responsible for the observed low velocities in the uppermost several kilometers beneath the LRZ, which is underlain by a layer of Permo-Triassic clastic sediments (Banks et al., 1995) and is characterized by negative Bouguer gravity anomalies (Fig. 2a). Another contributing factor for the low velocities beneath the MRZ and LRZ is deep penetrating faults (e.g., Yu et al., 2015 for the Okavango Rift), whose existence is suggested by the frequent occurrence of earthquakes.
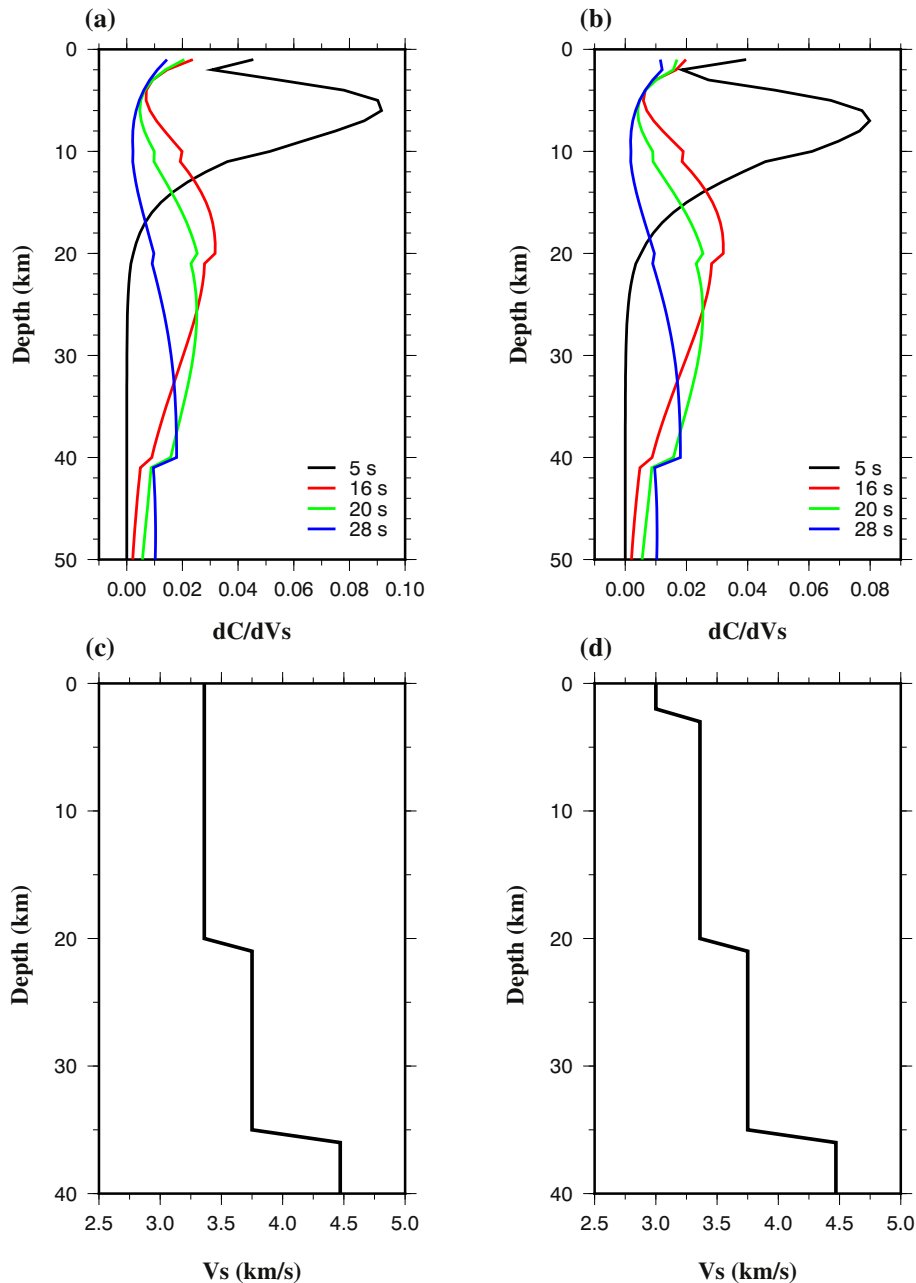
Fig. 5. Shear wave sensitivity kernels for Rayleigh wave phase velocities at different periods and initial models for the inversion of shear wave velocities. (a) Sensitivity curves calculated based on the IASP91 Earth model. C is the phase velocity and V_s is the shear wave velocity. (b) Same as (a), but with a 2 km low velocity layer (3 km/s) to reflect the loose sediments. (c) Initial model generated based on the IASP91 Earth model. (d) Same as (c), but a low velocity layer (3 km/s) is added to replace the uppermost 2 km of the IASP91 model.

Higher than normal crustal temperatures can also contribute to the observed low seismic velocities in the crust. The relatively high heat flow values (about 77 mW m^{-2}) and the numerous hot springs in the MRZ (Gondwe et al., 2012; Njinju et al., 2015) are indicative of a higher than normal crustal temperature. If we assume that the temperature beneath the SIB at 25 km depth is 350 °C, which is comparable to that of a typical cratonic area (Blackwell, 1971), the observed heat flow value of 67 mW m^{-2} in the SIB (Njinju et al., 2015) suggests an average thermal conductivity of 4.79 W m^{-1} °C^{-1}, a value that is typical for crustal rocks (Birch and Clark, 1940). Interpreting seismic velocity within the crust in terms of temperature is inherently complicated owing to non-linear relationships between composition, density, and temperature for crustal rocks. Therefore, a certain degree of uncertainty exists in the crustal temperatures.

The V_s beneath the MRZ at the depth of 25 km is about 0.13 km/s slower than that beneath the SIB (Fig. 8). Under the assumption that the observed low V_s anomaly in the MRZ is entirely thermally induced, the scaling relationship $\partial V_s/T = 0.35$ ms^{-1} K^{-1} (Sumino and Anderson, 1982) results in a temperature anomaly of about 370 °C (and thus a temperature of 720 °C) relative to the SIB (beneath which the assumed temperature is 350 °C at 25 km depth). Applying a thermal conductivity of 4.79 W m^{-1} °C^{-1} estimated above and a temperature of 720 °C at the depth of 25 km beneath the MRZ, the anticipated heat flow in the MRZ would be as high as 138 mW m^{-2}, which is about 60 mW m^{-2} higher than the observed value. Therefore, in spite of possible uncertainties in the assumed temperatures and temperature-velocity relationship, the large difference between the observed and predicted heat flow values suggests that temperature anomalies alone
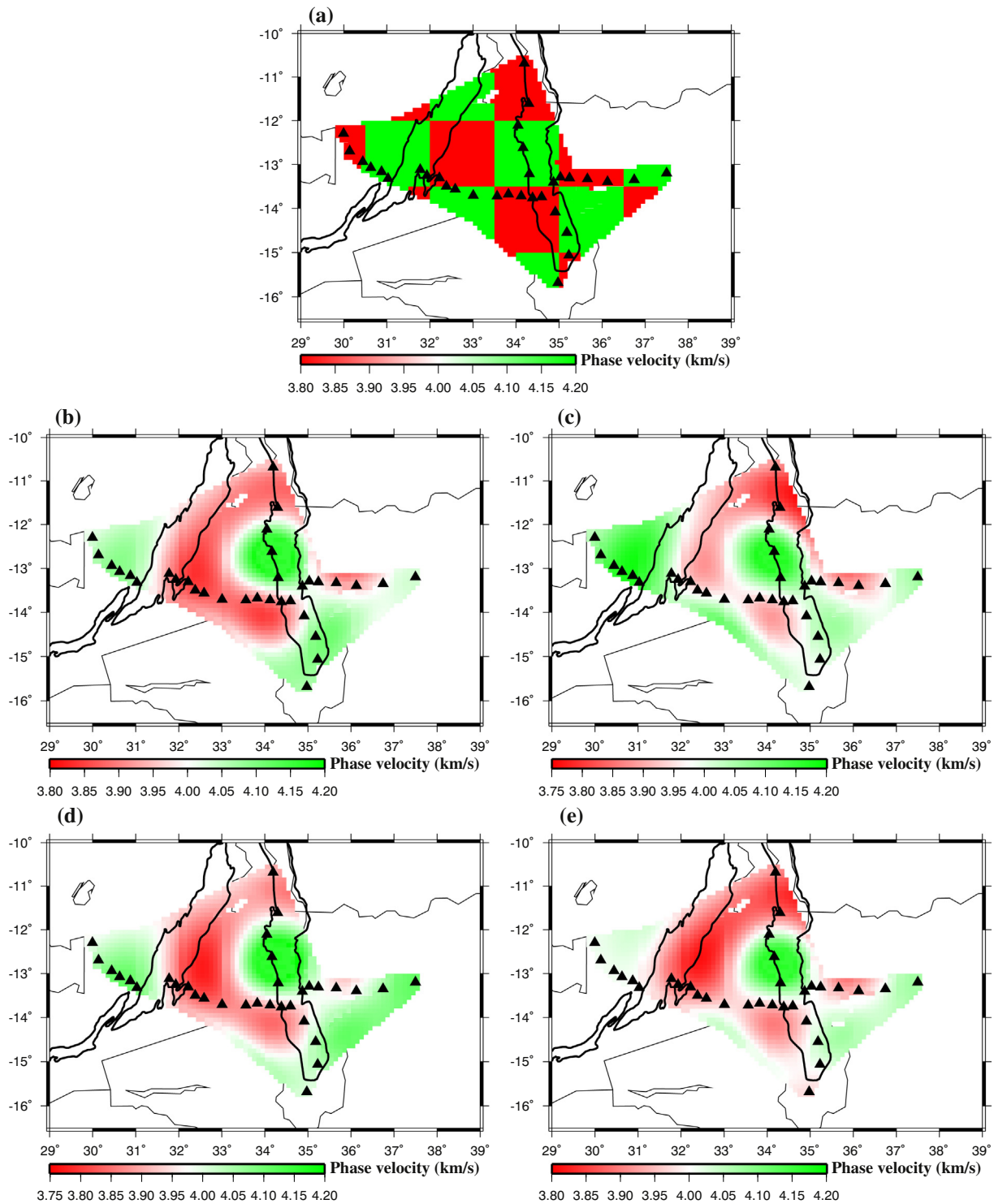
Fig. 6. Horizontal checkerboard model and its reconstructions at different periods. Stations are depicted with black triangles. The colors represent velocities with positive and negative 5% perturbations relative to a reference velocity of 4 km/s. (a) The input checkerboard model. (b)–(e) The recovered velocities for the periods of 5, 16, 20, and 28 s, respectively.

are insufficient to produce the observed low crustal velocities beneath the MRZ. Other factors, such as fluid-filled deep penetrating faults, partial melting, and possibly magmatic intrusion (Fagereng, 2013), may also be important factors for the observed low velocities.

4.2. Crustal thickness beneath the rifts

For typical stable cratonic areas, V_s ranges from 3.9 to 4.2 km/s in the lower crust, and over 4.2 km/s in the uppermost mantle

(e.g., Schulte-Pelkum et al., 2017; Shen et al., 2013a, 2013b; Shen and Ritzwoller, 2016). Based on these values, in the following we estimate the crustal thickness (H) from the resulting velocity models by considering V_s values of over 4.2 km/s as the velocities in the uppermost mantle, with the understanding that for a given location, the V_s measurements obtained using ANT represent the average over a vertical distance, and consequently, there is an uncertainty of a few kilometers in the estimated H results. Using a different threshold V_s value would result in different absolute crustal thicknesses, but the
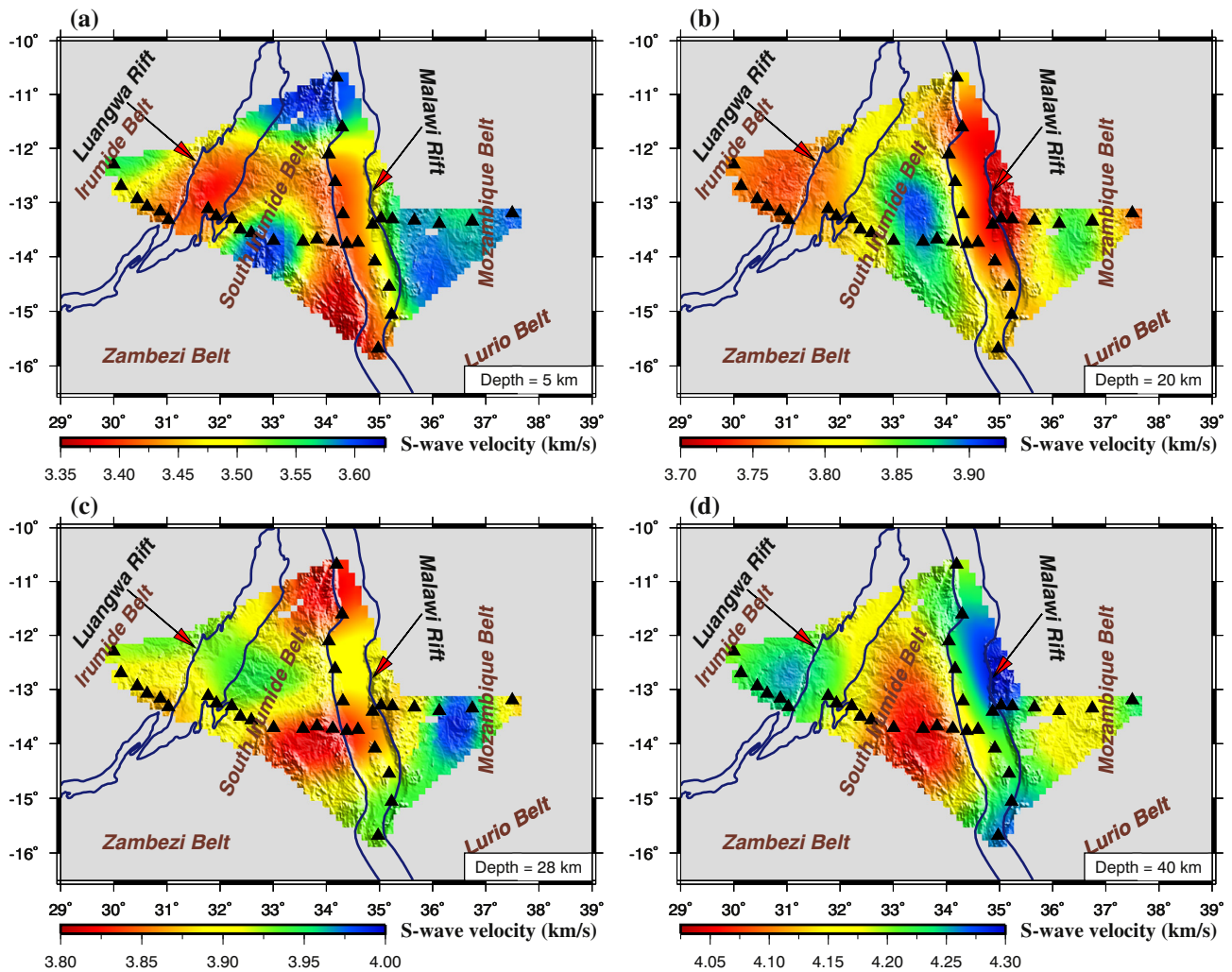
Fig. 7. Horizontal shear wave velocity slices at different depths. (a) 5 km. (b) 20 km. (c) 28 km. (d) 40 km.

relative magnitude of the topography of the Moho should not change significantly.

The V_s slice map at the depth of 40 km (Fig. 7d) shows velocities that are higher than 4.2 km/s beneath most of the MRZ and the central part of the LRZ, suggesting that crustal thickness beneath the rifts is <40 km. To obtain more detailed estimates of the crustal thickness, we plot V_s slices at the depths of 32–38 km with an interval of 2 km (Fig. 10). At the depth of 38 km (Fig. 10d), shear wave velocities beneath the LRZ are lower than 4.2 km/s, which, when combined with the results at the depth of 40 km (Fig. 7d), indicate that the crustal thickness beneath the LRZ is most likely between 38 and 40 km. Shear wave velocities beneath the MRZ reach about 4.2 km/s at the depth of 38 km but are lower than 4.2 km/s at the depth of 36 km, implying that the Moho depth is between 36 and 38 km beneath most part of the MRZ, except for the section between 13°S and 15°S latitudes, where a thicker crust with a depth between 38 and 40 km is present. Note that the accuracy of the estimated crustal thickness variations is dependent on uncertainties in crustal velocities. The resulting crustal thinning beneath both rifts is significantly smaller than the Tanganyika Rift that is also part of the western branch of the EARS, beneath which ~20% thinning is suggested (Hodgson et al., 2017).

The mean shear wave velocities beneath the SIB and the Mozambique Belt at the depth of 40 km are both lower than 4.2 km/s (Figs. 7d and 8), indicating that H is >40 km beneath both orogenic belts, a conclusion that is consistent with previous crustal thickness observations obtained at several points using receiver functions (Kachingwe et al., 2015).

4.3. Comparison with other continental rifts

To put the resulting H and V_s observations obtained beneath the MRZ and LRZ in a global context, we compare the H and V_s measurements at the mid-crustal depth of 20 km, which is termed as $V_s(20)$, observed beneath the MRZ and LRZ with those obtained at major Cenozoic continental rift zones elsewhere (Fig. 11). The particular depth is at approximately the middle of the crust and thus minimizes the influence of velocity heterogeneities in the top-most layer, as well as magmatic underplating or eclogitization that is common for the lower crust (Baird et al., 1995). For a given rift, H and $V_s(20)$ are taken at the location where the crust is the thinnest. For the Baikal Rift Zone (BRZ), and the central and southern segments of the Kenya Rift (CKR and SKR, respectively), only P-wave velocities are available, and consequently, $V_s(20)$ is taken as $V_p(20)/1.78$ where $V_p(20)$ is the P-wave velocity at 20 km depth, and 1.78 is the mean crustal V_p/V_s (Christensen, 1996). For the Main Ethiopian Rift (MER), the results from the active-source seismic study of Mackenzie et al. (2005) are used instead of those produced by other lower-resolution techniques (e.g., Kim et al., 2012).

The receiver function study at the BRZ (Gao et al., 2004) reported a minimum crustal thickness of 35 km and suggested significant crustal thinning relative to the neighboring Siberian Platform. In contrast, an
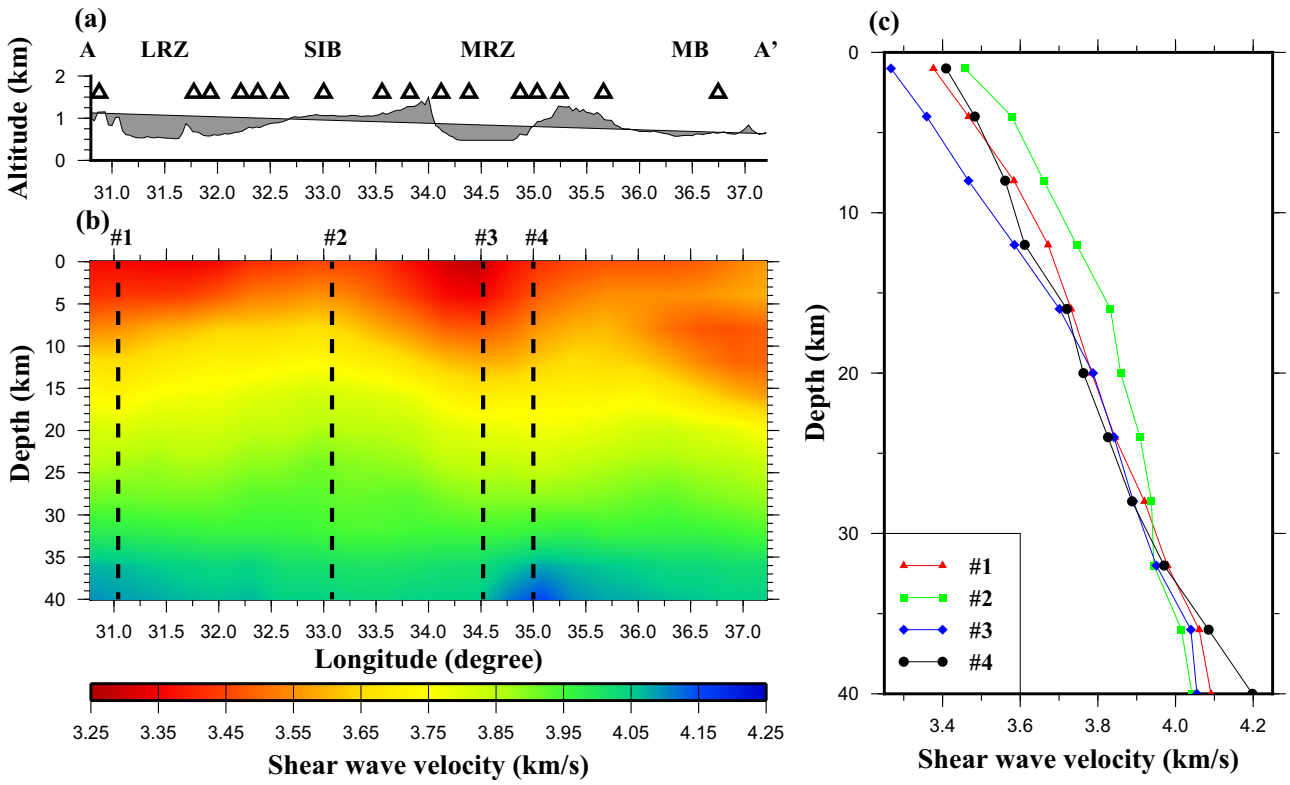
Fig. 8. (a) Surface elevation and major geological features along W-E Profile A–A′ shown in Fig. 1. Triangles are seismic stations. MB: Mozambique Belt. (b) Shear wave velocities along the profile. (c) Depth variation of shear wave velocities extracted from the black dashed lines in (b).

active-source seismic reflection survey (Thybo and Nielsen, 2009) suggested the existence of a high-velocity layer at the depth range of about 30–40 km and attributed it to magmatic intrusions into the lower crust that compensate the expected crustal thinning. Given the inconsistencies between the two results, the BRZ is represented by two points in Fig. 11, where BRZ01 is based on the active source seismic
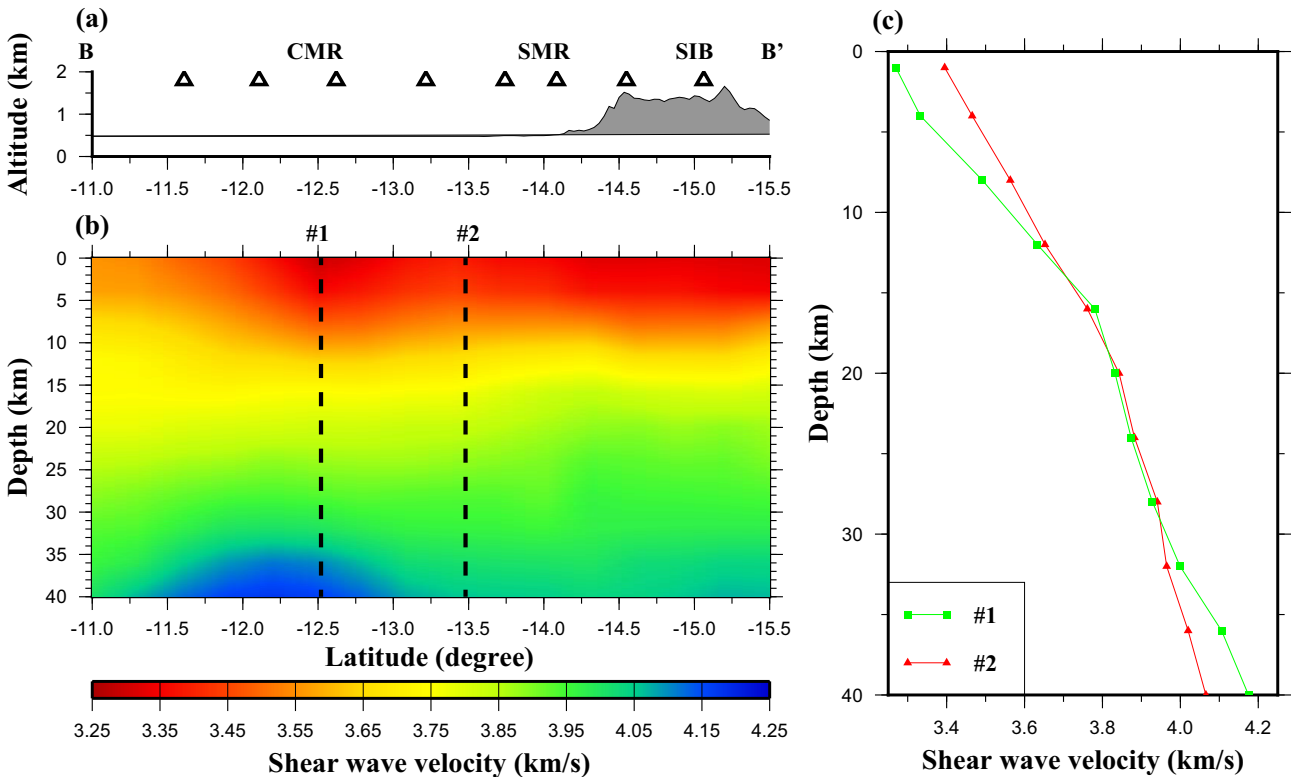
Fig. 9. Same as Fig. 8 but for N-S Profile B–B′ shown in Fig. 1. CMR: Central Malawi Rift. SMR: Southern Malawi Rift.
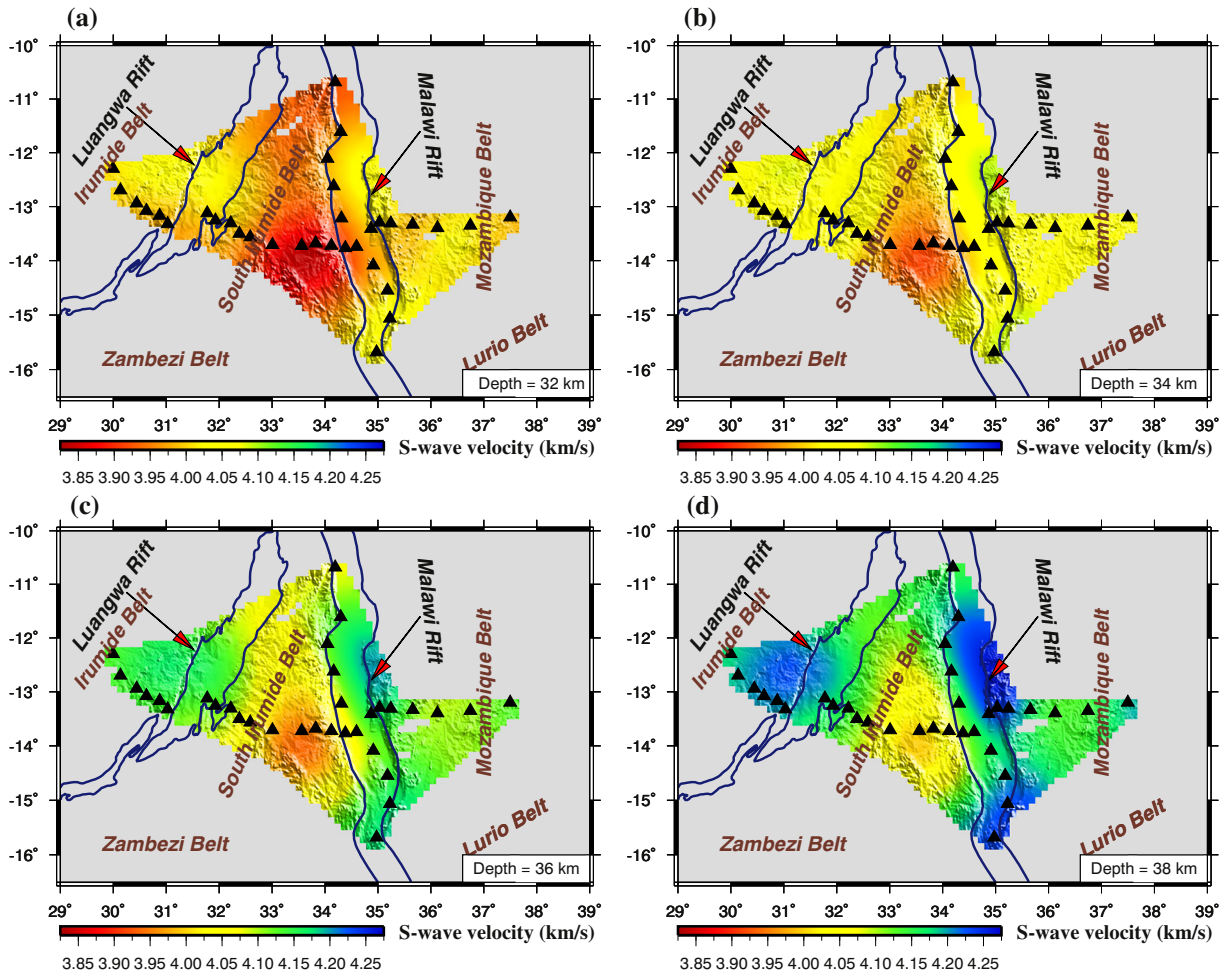
Fig. 10. Horizontal shear wave velocity slices at different depths. (a) 32 km. (b) 34 km. (c) 36 km. (d) 38 km.

study (Thybo and Nielsen, 2009), and the crustal thickness of BRZ02 is from the receiver function study (Gao et al., 2004) while the corresponding $V_s(20)$ is taken from the active source seismic survey.

A positive correlation between H and $V_s(20)$ is observed (Fig. 11), suggesting that crustal extension leads to reduction of crustal velocities that is attributable to temperature increase, existence of partial melting, magmatic intrusion, and the development of crustal scale boundary faults. On the basis of the relationship shown in Fig. 11, the rifts can be divided into three categories. Those in the first category (red ellipse; Fig. 11) include the MER and the CKR and the SKR belonging to the eastern branch of the EARS. A 2-D wide-angle seismic reflection/refraction modeling is utilized to calculate H and $V_s(20)$ values beneath the MER. Information of H and $V_s(20)$ for the CKR and the SKR is obtained from a combined analysis of seismic refraction and gravity data. The crustal thickness beneath those rifts is 32 km or less, and $V_s(20)$ is ≤3.74 km/s. A common feature of the rifts in this category is the pervasive presence of rifting-related volcanism (Keller et al., 1991). The second category (gray ellipse; Fig. 11) includes the BRZ if we assume that the Moho is beneath the high-velocity layer revealed by seismic reflection data (Thybo and Nielsen, 2009). However, if we assume that this layer is an underplated layer beneath the Moho, BRZ01, which is an apparent outlier on the H-$V_s(20)$ plot (Fig. 11), becomes consistent with the rest of the rifts. The third category (green ellipse; Fig. 11) includes the MRZ and LRZ investigated in this study, the Shanxi Rift Zone (SRZ) in northern China, the Rio Grande Rift (RGR) in North America, and the BRZ02 if the receiver function results (Gao et al., 2004) are utilized. For the SRZ, H and $V_s(20)$ measurements are from the technique of ANT. Velocity information beneath the RGR is

from ANT method, while the H value is calculated by a receiver function study. The crust thickness beneath these rifts is ≥34 km with a $V_s(20)$ that is higher than those in the first category. These rifts are
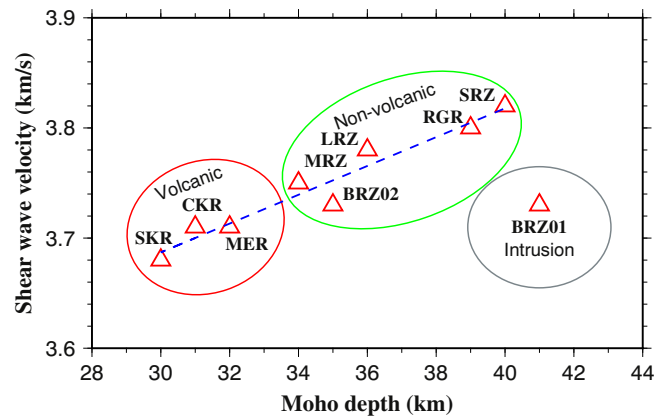

Fig. 11. A compilation of Moho depths and shear wave velocities at the depth of 20 km beneath the world's major continental rift zones. CKR: Central Kenya Rift (Maguire et al., 1994); MER: Main Ethiopian Rift (Mackenzie et al., 2005); RGR: Rio Grande Rift (Fu and Li, 2015; Gilbert, 2012); SKR: Southern Kenya Rift (Birt et al., 1997); SRZ: Shanxi Rift Zone (Song et al., 2015); BRZ01: Baikal Rift Zone (Thybo and Nielsen, 2009); BRZ02: Baikal Rift Zone (Gao et al., 2004; Thybo and Nielsen, 2009). The blue dashed line is the line of best fit of all the data points excluding BRZ01, and the ellipses divide the rifts into three categories (see text for details). (For interpretation of the references to color in this figure legend, the reader is referred to the web version of this article.)

characterized by an absence or limited volcanism (Logatchev and Florensov, 1978; Keller et al., 1991).

Fig. 11 suggests that volcanism is closely related to the magnitude of crustal thinning. Indeed, except for the Rungwe Volcanic Province at its northern terminus, the MRZ is non-volcanic, indicating that the crust beneath the young rift has not been thinned to the threshold value below which volcanism can develop. This nevertheless does not exclude the possibility of igneous intrusion into the lower or even the upper crust, as evidenced by the lower than normal shear wave velocities observed beneath the rift (Fig. 8).

Although it is tectonically inactive at the present time, the LRZ also possesses a thinner crust relative to the surrounding area, and no rift-related volcanic activities have been reported (Sarafian et al., 2018), similarly suggesting that crustal extension responsible for creating the Permo-Triassic rift did not reach the point of producing volcanism. The lower than normal V_s in the upper crust observed beneath the LRZ may suggest that crustal temperature remains higher than normal over the past 250 million years since the cessation of the rifting process, which is unlikely. Alternatively, it may suggest reactivation of the failed rift (Daly et al., 1989; Banks et al., 1995).

5. Conclusion

We implement ambient noise tomography to construct Rayleigh wave phase velocity maps in the vicinity of the MRZ, LRZ, SIB, and portions of the Mozambique and Irumide Belts in southern Africa using a recently-recorded broadband seismic data set. Dispersion measurements are extracted from these phase velocity maps and are inverted to construct the first 3-D crustal shear wave velocity model for the area, which reveals that relative to the neighboring areas, the MRZ and LRZ are characterized by low velocity anomalies in the mid-crust, probably as the results of a combination of multiple factors including positive temperature anomaly, fluid-filled deep faults, partial melting, and magmatic intrusion. Thinning of the crust beneath both the MRZ and LRZ of a few km is inferred from the horizontal velocity slices. The observed crustal thicknesses and seismic velocities beneath the non-volcanic MRZ and LRZ are consistent with other non-volcanic continental rifts on Earth, and suggest that the crust has not been adequately thinned to enable the development of syn-rifting volcanism.

References

Accardo, N.J., Gaherty, J.B., Shillington, D.J., Ebinger, C.J., Nyblade, A.A., Mbogoni, G.J., Chindandali, P.R.N., Ferdinand, R.W., Mulibo, G.D., Kamihanda, G., Keir, D., Scholz, C., Selway, K., O'Donnell, J.P., Tepp, G., Gallacher, R., Mtelela, K., Salima, J., Mruma, A., 2017. Surface wave imaging of the weakly extended Malawi Rift from ambient-noise and teleseismic Rayleigh waves from onshore and lake-bottom seismometers. Geophysical Journal International 209 (3), 1,892–1,905. https://doi.org/10.1093/gji/ggx133.

Baird, D.J., Knapp, J.H., Steer, D.N., Brown, L.D., Nelson, K.D., 1995. Upper-mantle reflectivity beneath the Williston Basin, phase-change Moho, and the origin of intracratonic basins. Geology 23 (5), 431–434. https://doi.org/10.1130/0091-7613(1995)023<0431:UMRBTW>2.3.CO;2.

Banks, N.L., Bardwell, K.A., Musiwa, S., 1995. Karoo rift basins of the Luangwa valley, Zambia. In: Lambiase, J.J. (Ed.), Hydrocarbon Habitat in Rift Basins. Geological Society, London, Special Publications vol. 80(1), pp. 285–295. https://doi.org/10.1144/GSL.SP.1995.080.01.13.

Bensen, G.D., Ritzwoller, M.H., Barmin, M.P., Levshin, A.L., Lin, F.-C., Moschetti, M.P., Shapiro, N.M., Yang, Y., 2007. Processing seismic ambient noise data to obtain reliable broad-band surface wave dispersion measurements. Geophysical Journal International 169 (3), 1,239–1,260. https://doi.org/10.1111/j.1365-246X.2007.03374.x.

Betzler, C., Ring, U., 1995. Sedimentology of the Malawi Rift: facies and stratigraphy of the Chiwondo Beds, northern Malawi. Journal of Human Evolution 28 (1), 23–35. https://doi.org/10.1006/jhev.1995.1004.

Birch, A.F., Clark, H., 1940. The thermal conductivity of rocks and its dependence upon temperature and composition. American Journal of Science 238 (8), 529–558. https://doi.org/10.2475/ajs.238.8.529.

Birt, C.S., Maguire, P.K.H., Khan, M.A., Thybo, H., Keller, G.R., Patel, J., 1997. The influence of pre-existing structures on the evolution of the southern Kenya Rift valley-evidence from seismic and gravity studies. Tectonophysics 278 (1–4), 211–242. https://doi.org/10.1016/S0040-1951(97)00105-4.

Blackwell, D.D., 1971. The thermal structure of the continental crust. In: Heacock, J.G. (Ed.), The Structure and Physical Properties of the Earth's Crust. Geophysical Monograph 14, pp. 169–184.

Borrego, D., Nyblade, A.A., Accardo, N.J., Gaherty, J.B., Ebinger, C.J., Shillington, D.J., Chindandali, P.R.N., Mbogoni, G., Ferdinand, R.W., Mulibo, G., O'Donnell, J.P., Kachingwe, M., Tepp, G., 2018. Crustal structure surrounding the northern Malawi rift and beneath the Rungwe Volcanic Province, East Africa. Geophysical Journal International 215 (2), 1,410–1,426. https://doi.org/10.1093/gji/ggy331.

Christensen, N.I., 1996. Poisson's ratio and crustal seismology. Journal of Geophysical Research - Solid Earth 101 (B2), 3,139–3,156. https://doi.org/10.1029/95JB03446.

Craig, T.J., Jackson, J.A., Priestley, K., McKenzie, D., 2011. Earthquake distribution patterns in Africa: their relationship to variations in lithospheric and geological structure, and their rheological implications. Geophysical Journal International 185 (1), 403–434. https://doi.org/10.1111/j.1365-246X.2011.04950.x.

Daly, M.C., Chorowicz, J., Fairhead, J.D., 1989. Rift basin evolution in Africa: the influence of reactivated steep basement shear zones. In: Cooper, M.A., Williams, G.D. (Eds.), Inversion Tectonics. Geological Society, London, Special Publications vol. 44, pp. 309–334. https://doi.org/10.1144/GSL.SP.1989.044.01.17.

Druken, K.A., Kincaid, C., Griffiths, R.W., 2013. Directions of seismic anisotropy in laboratory models of mantle plumes. Geophysical Research Letters 40 (14), 3,544–3,549. https://doi.org/10.1002/grl.50671.

Ebinger, C.J., Rosendahl, B.R., Reynolds, D.J., 1987. Tectonic model of the Malawi rift, Africa. Tectonophysics 141 (1–3), 215–235. https://doi.org/10.1016/0040-1951(87)90187-9.

Ebinger, C.J., Deino, A.L., Drake, R.E., Tesha, A.L., 1989. Chronology of volcanism and rift basin propagation: Rungwe volcanic province, East Africa. Journal of Geophysical Research - Solid Earth 94 (B11), 15,785–15,803. https://doi.org/10.1029/JB094iB11p15785.

Fagereng, A., 2013. Fault segmentation, deep rift earthquakes and crustal rheology: insights from the 2009 Karonga sequence and seismicity in the Rukwa-Malawi rift zone. Tectonophysics 601, 216–225. https://doi.org/10.1016/j.tecto.2013.05.012.

Flannery, J.W., Rosendahl, B.R., 1990. The seismic stratigraphy of Lake Malawi, Africa: implications for interpreting geological processes in lacustrine rifts. Journal of African Earth Sciences 10 (3), 519–548. https://doi.org/10.1016/0899-5362(90)90104-M.

Fritz, H., Abdelsalam, M., Ali, K.A., Bingen, B., Collins, A.S., Fowler, A.R., Ghebreab, W., Hauzenberger, C.A., Johnson, P.R., Kusky, T.M., Macey, P., Muhongo, S., Stern, R.J., Viola, J., 2013. Orogen styles in the East African Orogen: a review of the Neoproterozoic to Cambrian tectonic evolution. Journal of African Earth Sciences 86, 65–106. https://doi.org/10.1016/j.jafrearsci.2013.06.004.

Fu, Y.V., Li, A., 2015. Crustal shear wave velocity and radial anisotropy beneath the Rio Grande rift from ambient noise tomography. Journal of Geophysical Research - Solid Earth 120 (2), 1,005–1,019. https://doi.org/10.1002/2014JB011602.

Gao, S., Davis, P.M., Liu, H., Slack, P.D., Zorin, Yu.A., Mordvinova, V.V., Kozhevnikov, V.M., Meyer, R.P., 1994. Seismic anisotropy and mantle flow beneath the Baikal rift zone. Nature 371, 149–151. https://doi.org/10.1038/371149a0.

Gao, S., Davis, P.M., Liu, H., Slack, P.D., Rigor, A.W., Zorin, Y.A., Mordvinova, V.V., Kozhevnikov, V.M., Logatchev, N.A., 1997. SKS splitting beneath continental rift zones. Journal of Geophysical Research - Solid Earth 102 (B10), 22,781–22,797. https://doi.org/10.1029/97JB01858.

Gao, S.S., Liu, K.H., Chen, C., 2004. Significant crustal thinning beneath the Baikal rift zone: new constraints from receiver function analysis. Geophysical Research Letters 31 (20), L20610. https://doi.org/10.1029/2004GL020813 1–4. https://doi.org/10.1029/2004GL020813.

Gao, S.S., Liu, K.H., Reed, C.A., Yu, Y., Massinque, B., Mdala, H., Moidaki, M., Mutamina, D., Atekwana, E.A., Ingate, S., Reusch, A.M., 2013. Seismic arrays to study African rift initiation. Eos, Transactions of the American Geophysical Union 94 (24), 213–214. https://doi.org/10.1002/2013EO240002.

Gilbert, H., 2012. Crustal structure and signatures of recent tectonism as influenced by ancient terranes in the Western United States. Geosphere 8 (1), 141–157. https://doi.org/10.1130/GES00720.1.

Gondwe, K., Allen, A., Georgsson, L.S., Loga, U., Tsokonombwe, G., 2012. Geothermal development in Malawi - A country update. paper presented at 4th African Rift Geothermal Conference, Geothermal Solutions to Africa's Energy Needs, UN Gigiri Complex, Nairobi, Kenya, Nairobi.

Herrmann, R.B., Ammon, C.J., 2004. Surface waves, receiver functions and crustal structure. Computer Programs in Seismology, VERSION 3.30. Saint Louis University.

Hodgson, I., Illsley-Kemp, F., Gallacher, R.J., Keir, D., Ebinger, C.J., Mtelela, K., 2017. Crustal structure at a young continental rift: a receiver function study from the Tanganyika Rift. Tectonics 36 (12), 2,806–2,822. https://doi.org/10.1002/2017TC004477.

Kachingwe, M., Nyblade, A., Julia, J., 2015. Crustal structure of Precambrian terranes in the southern African subcontinent with implications for secular variation in crustal genesis. Geophysical Journal International 202 (1), 533–547. https://doi.org/10.1093/gji/ggv136.

Keller, G.R., Khan, M.A., Morganc, P., Wendlandt, R.F., Baldridge, W.S., Olsen, K.H., Prodehl, C., Braile, L.W., 1991. A comparative study of the Rio Grande and Kenya rifts. Tectonophysics 197 (2–4), 355–371. https://doi.org/10.1016/0040-1951(91)90050-3.

Kennett, B.L.N., Engdahl, E.R., 1991. Traveltimes for global earthquake location and phase identification. Geophysical Journal International 105 (2), 429–465. https://doi.org/10.1111/j.1365-246X.1991.tb06724.x.

Kim, S., Nyblade, A.A., Baag, C.-E., 2009. Crustal velocity structure of the Rukwa Rift in the Western Branch of the east African rift system. South African Journal of Geology 112 (3–4), 251–260. https://doi.org/10.2113/gssajg.112.3-4.251.

Kim, S., Nyblade, A.A., Rhie, J., Baag, C.-E., Kang, T.-S., 2012. Crustal S-wave velocity structure of the Main Ethiopian Rift from ambient noise tomography. Geophysical Journal International 191 (2), 865–878. https://doi.org/10.1111/j.1365-246X.2012.05664.x.

Lao-Davila, D.A., Al-Salmi, H.S., Abdelsalam, M.G., Atekwana, E.A., 2015. Hierarchical segmentation of the Malawi Rift: the influence of inherited lithospheric heterogeneity and kinematics in the evolution of continental rifts. Tectonics 34 (12), 2,399–2,417. https://doi.org/10.1002/2015TC003953.

Laske, G., Masters, G., Ma, Z., Pasyanos, M., 2013. Update on CRUST1.0 - a 1-degree global model of Earth's crust. Geophys. Res. Abstr. 15. EGU, pp. 2,013–2,658.

Lin, F.-C., Moschetti, M.P., Ritzwoller, M.H., 2008. Surface wave tomography of the western United States from ambient seismic noise: Rayleigh and Love wave phase velocity maps. Geophysical Journal International 173 (1), 281–298. https://doi.org/10.1111/j.1365-246X.2008.03720.x.

Logatchev, N.A., Florensov, N.A., 1978. The Baikal system of rift valleys. Tectonophysics 45 (1), 1–13. https://doi.org/10.1016/0040-1951(78)90218-4.

Mackenzie, G.D., Thybo, H., Maguire, P.K.H., 2005. Crustal velocity structure across the Main Ethiopian Rift: results from two-dimensional wide-angle seismic modelling. Geophysical Journal International 162 (3), 994–1,006. https://doi.org/10.1111/j.1365-246X.2005.02710.x.

Maguire, P.K.H., Swain, C.J., Masotti, R., Khan, M.A., 1994. A crustal and uppermost mantle cross-sectional model of the Kenya Rift derived from seismic and gravity data. Tectonophysics 236 (1–4), 217–249. https://doi.org/10.1016/0040-1951(94)90178-3.

Njinju, E.A., Atekwana, E.A., Mickus, K.L., Lao-Davila, D.A., Abdelsalam, M.G., Atekwana, E.A., 2015. Geophysical investigation of thermal structures beneath the Malawi rift. SEG Technical Program Expanded Abstracts 2015, pp. 1578–1583.

Nolet, G., Dahlen, F.A., 2000. Wave front healing and the evolution of seismic delay times. Journal of Geophysical Research - Solid Earth 105 (B8), 19,043–19,054. https://doi.org/10.1029/2000JB900161.

Reed, C.A., Liu, K.H., Chindandali, P.R.N., Massingue, B., Mdala, H., Mutamina, D., Yu, Y., Gao, S.S., 2016. Passive rifting of thick lithosphere in the southern East African Rift: evidence from mantle transition zone discontinuity topography. Journal of Geophysical Research - Solid Earth 121 (11), 8,068–8,079. https://doi.org/10.1002/2016JB013131.

Reed, C.A., Liu, K.H., Yu, Y., Gao, S.S., 2017. Seismic anisotropy and mantle dynamics beneath the Malawi Rift Zone, East Africa. Tectonics 36 (7), 1,338–1,351. https://doi.org/10.1002/2017TC004519.

Ritzwoller, M.H., Levshin, A.L., 1998. Eurasian surface wave tomography: group velocities. Journal of Geophysical Research - Solid Earth 103 (B3), 4,839–4,878. https://doi.org/10.1029/97JB02622.

Ritzwoller, M.H., Shapiro, N.M., Barmin, M.P., Levshin, A.L., 2002. Global surface wave diffraction tomography. Journal of Geophysical Research-Solid Earth 107 (B12), ESE 4-1-ESE 4-13. https://doi.org/10.1029/2002JB001777.

Roberts, E.M., Stevens, N.J., O'Connor, P.M., Dirks, P.H.G.M., Gottfried, M.D., Clyde, W.C., Armstrong, R.A., Kemp, A.I.S., Hemming, S., 2012. Initiation of the western branch of the East African Rift coeval with the eastern branch. Nature Geoscience 5 (4), 289–294. https://doi.org/10.1038/ngeo1432.

Sabra, K.G., Gerstoft, P., Roux, P., Kuperman, W.A., Fehler, M.C., 2005. Extracting time-domain Green's function estimates from ambient seismic noise. Geophysical Research Letters 32 (3), 1–5. https://doi.org/10.1029/2004GL021862.

Sarafian, E., Evans, R.L., Abdelsalam, M.G., Atekwana, E., Elsenbeck, J., Jones, A.G., Chikambwe, E., 2018. Imaging Precambrian lithospheric structure in Zambia using electromagnetic methods. Gondwana Research 54, 38–49. https://doi.org/10.1016/j.gr.2017.09.007.

Schulte-Pelkum, V., Mahan, K.H., Shen, W., Stachnik, J.C., 2017. The distribution and composition of high-velocity lower crust across the continental U.S.: comparison of seismic and xenolith data and implications for lithospheric dynamics and history. Tectonics 36 (8), 1,455–1,496. https://doi.org/10.1002/2017TC004480.

Sengor, A.M.C., Burke, K., 1978. Relative timing of rifting and volcanism on Earth and its tectonic implications. Geophysical Research Letters 5 (6), 419–421. https://doi.org/10.1029/GL005i006p00419.

Shapiro, N.M., Campillo, M., 2004. Emergence of broadband Rayleigh waves from correlations of the ambient seismic noise. Geophysical Research Letters 31 (7), 1–4. https://doi.org/10.1029/2004GL019491.

Shapiro, N.M., Ritzwoller, M.H., 2002. Monte-Carlo inversion for a global shear velocity model of the crust and upper mantle. Geophysical Journal International 151 (1), 88–105. https://doi.org/10.1046/j.1365-246X.2002.01742.x.

Shapiro, N.M., Campillo, M., Stehly, L., Ritzwoller, M.H., 2005. High-resolution surface-wave tomography from ambient seismic noise. Science 307 (5715), 1,615–1,618. https://doi.org/10.1126/science.1108339.

Shen, W., Ritzwoller, M.H., 2016. Crustal and uppermost mantle structure beneath the United States. Journal of Geophysical Research - Solid Earth 121 (6), 4,306–4,342. https://doi.org/10.1002/2016JB012887.

Shen, W., Ritzwoller, M.H., Schulte-Pelkum, V., 2013a. A 3-D model of the crust and uppermost mantle beneath the central and western US by joint inversion of receiver functions and surface wave dispersion. Journal of Geophysical Research - Solid Earth 118 (1), 262–276. https://doi.org/10.1029/2012JB009602.

Shen, W., Ritzwoller, M.H., Schulte-Pelkum, V., Lin, F.-C., 2013b. Joint inversion of surface wave dispersion and receiver functions: a Bayesian Monte-Carlo approach. Geophysical Journal International 192 (2), 807–836. https://doi.org/10.1093/gji/ggs050.

Song, M., Zheng, Y., Liu, C., Li, L., Wang, X., 2015. Shear-wave velocity structure of the crust and uppermost mantle in the Shanxi rift zone. Earthquake Science 28 (2), 135–149. https://doi.org/10.1007/s11589-015-0117-0.

Specht, T.D., Rosendahl, B.R., 1989. Architecture of the Lake Malawi rift, East Africa. Journal of African Earth Sciences 8 (2–4), 355–382. https://doi.org/10.1016/S0899-5362(89)80032-6.

Spetzler, J., Trampert, J., Snieder, R., 2002. The effect of scattering in surface wave tomography. Geophysical Journal International 149 (3), 755–767. https://doi.org/10.1046/j.1365-246X.2002.01683.x.

Sumino, Y., Anderson, O.L., 1982. Elastic constants in minerals. In: Carmichel, R.S. (Ed.), CRC Handbook of Physical Properties of Rocks. CRC Press, Boca Raton, FL, pp. 39–138.

Tarantola, A., Nercessian, A., 1984. Three-dimensional inversion without blocks. Geophysical Journal International 76 (2), 299–306. https://doi.org/10.1111/j.1365-246X.1984.tb05047.x.

Tarantola, A., Valette, B., 1982. Generalized nonlinear inverse problem solved using the least squares criterion. Reviews of Geophysics and Space Physics 20 (2), 219–232. https://doi.org/10.1029/RG020i002p00219.

Thybo, H., Nielsen, C.A., 2009. Magma-compensated crustal thinning in continental rift zones. Nature 457 (7231), 873–876. https://doi.org/10.1038/nature07688.

Tugume, F.A., Nyblade, A.A., Julià, J., 2012. Moho depths and Poisson's ratios of Precambrian crust in East Africa: evidence for similarities in Archean and Proterozoic crustal structure. Earth and Planetary Science Letters 355-356, 73–81. https://doi.org/10.1016/j.epsl.2012.08.041.

Walker, K.T., Bokelmann, G.H.R., Klemperer, S.L., 2001. Shear-wave splitting to test mantle deformation models around Hawaii. Geophysical Research Letters 28 (22), 4,319–4,322. https://doi.org/10.1029/2001GL013299.

Weaver, R.L., 2005. Information from seismic noise. Science 307 (5715), 1,568–1,569. https://doi.org/10.1126/science.1109834.

Weaver, R.L., Lobkis, O.I., 2004. Diffuse fields in open systems and the emergence of the Green's function. The Journal of the Acoustical Society of America 116 (5), 2,731–2,734. https://doi.org/10.1121/1.1810232.

Yang, Y., Zheng, Y., Chen, J., Zhou, S., Celyan, S., Sandvol, E., Tilmann, F., Priestley, K., Hearn, T.M., Ni, J.F., Brown, L.D., Ritzwooler, M.H., 2010. Rayleigh wave phase velocity maps of Tibet and the surrounding regions from ambient seismic noise tomography. Geochemistry, Geophysics, Geosystems 11 (8), Q08010. https://doi.org/10.1029/2010GC003119.

Yao, H., Xu, G., Zhu, L., Xiao, X., 2005. Mantle structure from inter-station Rayleigh wave dispersion and its tectonic implication in western China and neighboring regions. Physics of the Earth and Planetary Interiors 148 (1), 39–54. https://doi.org/10.1016/j.pepi.2004.08.006.

Yao, H., van der Hilst, R.D., de Hoop, M.V., 2006. Surface-wave array tomography in SE Tibet from ambient seismic noise and two-station analysis - I. Phase velocity maps. Geophysical Journal International 166 (2), 732–744. https://doi.org/10.1111/j.1365-246X.2006.03028.x.

Yao, H., van der Hilst, R.D., Montagner, J.-P., 2010. Heterogeneity and anisotropy of the lithosphere of SE Tibet from surface wave array tomography. Journal of Geophysical Research - Solid Earth 115 (B12), B12307. https://doi.org/10.1029/2009JB007142.

Yu, Y., Liu, K.H., Reed, C.A., Moidaki, M., Mickus, K., Atekwana, E.A., Gao, S.S., 2015. A joint receiver function and gravity study of crustal structure beneath the incipient Okavango Rift, Botswana. Geophysical Research Letters 42 (20), 8,398–8,405. https://doi.org/10.1002/2015GL065811.